Abdelmalek KRIBA [1], Farid MECHIGHEL [1,2]

Three-dimensional numerical study of the behavior of thermoelectric and mechanical coupling during spark plasma sintering of a polycrystalline material

Spark plasma sintering (SPS) is a promising modern technology that sinters a powder, whether it is ceramic or metallic, transforming it into a solid. This technique applies both mechanical pressure and a pulsed direct electric current simultaneously. This study presents a three-dimensional (3D) numerical investigation of the thermoelectric (thermal and electric current density fields) and mechanical (strain-stress and displacement fields) couplings during the SPS process of two powders: alumina (ceramic) and copper (metallic). The ANSYS software was employed to solve the conservation equations for energy, electric potential, and mechanical equilibrium simultaneously. Initially, the numerical findings regarding the thermoelectric and mechanical coupling phenomena observed in the alumina and copper specimens were compared with existing numerical and experimental results from the literature. Subsequently, a comprehensive analysis was conducted to examine the influence of current intensity and applied pressure on the aforementioned coupling behavior within the SPS device. The aim was to verify and clarify specific experimental values associated with these parameters, as reported in the literature, and identify the optimal values of applied pressure (5 MPa for alumina and 8.72 MPa for copper) and electric current (1000 A for alumina and 500 A for copper) to achieve a more homogeneous material.

✉ Abdelmalek KRIBA, e-mail: kriba.abdelmalek@univ-annaba.org

[1]Mechanics of Materials and Industrial Maintenance Research Laboratory (LR3MI), Mechanical Eng. Dept., Faculty of Technology, Badji Mokhtar University, 12. P.O.Box, 23000 Annaba, Algeria; ORCIDs: A.K.: 0009-0009-4219-5217, F.M.: 0000-0002-4726-7613

[2]Energy and Pollution Laboratory – Mentouri Brothers University – Constantine, Algeria

1. Introduction

Nowadays, spark plasma sintering attracts a lot of interest from many researchers because of its ability to sinter polycrystalline materials in a very short time (flash sintering) and with increased density (dense solids). This new sintering method among other techniques of the same family (such as field-activated sintering technique (FAST) or pulsed electric current sintering (PECS), etc.) uses a sintering system based on the simultaneous application of pulsed direct current (DC) and uniaxial mechanical pressure to enhance sintering.

The SPS process has many advantages over conventional processes (e.g., hot pressing (HP) or hot isostatic pressing (HIP)). Their main advantages are the remarkably reduced sintering time and temperature, which minimize grain *coarsening*, improve consolidation (densification) and often lead to *better* mechanical, thermal, physical and optical properties of the sintered material [1]. This is because the above properties (such as Young's modulus, Poisson's ratio, heat capacity, thermal conductivity, electrical resistivity, electrical conductivity, etc.) of the sintered material play an essential role in the SPS process [2]. Despite all these advantages, the SPS technique is however characterized by two major *drawbacks* which are the presence of *inhomogeneities* in the temperature distribution and in the distribution of mechanical stresses which can lead to inhomogeneities in the *microstructure* of the sample; especially in the case of a large sample, or a part having a shape close to that of a thread [3, 4]. Thus, the study and understanding of the behavior of thermoelectric and mechanical coupling in the SPS device (machine) is crucial in order to better manage and control the development of the SPS process. The study of the previous coupling can be done by studying the electric current density, the temperature and the mechanical stress-strain distributions in the system (composed of the components of the SPS device and the sintered sample) and their temporal evolutions. In this context, several analytical, experimental and/or numerical studies have been carried out. Among the relevant studies in the literature, one can distinguish, for example: the work of [5] presenting a finite element (FE) numerical simulation using ABAQUS and MATLAB software to determine the electric field and temperature distributions in the system during the SPS process of a graphite sample. The work of [6] presented a finite element model to simulate the behavior of thermoelectric, and mechanical coupling during an SPS process carried out at low temperature ($< 700°C$). In [1] the authors developed a finite element numerical procedure to simulate the temperature and stress distributions in an SPS device during the densification of an alumina powder sample. The authors performed thermoelectric analysis to understand the effects of applied pressure, electric current, and die size on the microstructure of the final product. In [7] the authors developed a finite element model using COMSOL software to simulate the SPS process of pure ultrafine tungsten carbide (WC) powder. The model includes a *moving* mesh technique to take into account the effects of contact resistances (CRs) which vary with the sliding of the punch. Although their model deals with the behavior of ther-

moelectric coupling, however, mechanical aspects such as stress-strain distributions have been neglected in the model. The work of [8] presented a numerical simulation by the finite element method (FEM) using a mathematical model that couples electrical, thermal and mechanical densification to model the SPS process of an alumina powder sample. They pointed out that the shape and size of the die have a significant effect on the distribution of the electric current density and that the latter being one of the factors responsible for the generation of heat (by Joule heating), and therefore of the resulting temperature distribution in the SPS device components and in the sample during the densification process. Their results also showed that the temperature distribution is more uniform in a cylindrical-shaped sample than in a cubic-shaped sample. The work of [9] performed a numerical simulation to study the effects of thermal contact resistances (TCRs) and electrical contact resistances (ECRs) between the interfaces (contact surfaces) of device components during the densification (SPS process) of the samples of titanium nitride (TiN) and zirconium dioxide (ZrO_2). The results showed that the temperature distribution in the system was closely related to the electrical properties of the sample; moreover, it is not homogeneous in the graphite die and inside the sample. In [10] the authors investigated powder-free (sample-free) SPS method to study thermal and electric fields with low strain and thermal expansion calibration. They found that contact resistances are one of the parameters that control the results of thermoelectric behavior in the SPS device. The work of [11] presented a simulation using the FEM method to study the effect of thermal gradient during field-activated sintering technique. They found that there is an approximately linear correlation between the surface temperature of the sample and the temperature distribution within the sample. They underlined the importance of evaluating the temperature distribution and studying the specific mechanisms of consolidation of the process, in order to optimize the processing parameters in the case of samples of large sizes. In [12] the authors carried out a numerical simulation to study the behavior of thermoelectric and mechanical coupling using ANSYS software during the SPS process of two types of samples (copper and alumina). The model assumes that the sample is a fully dense material and behaves like a linear elastic material. The model is applied to calculate the stress-strain distribution in the sample. In [4] the authors modeled numerically the thermoelectric and mechanical coupling using the COMSOL code during the SPS process of the alumina powder. Their objective was to analyze the influence of temperature on the coarsening of powder grains, and on the behavior of the powder densification process. In [13] the authors performed a numerical simulation of the thermoelectric and mechanical coupling using ABAQUS. Their model is based on a multiphysics analysis model of a lead sample with a decomposition of the strain rate tensorinto three elastic, thermal and viscoplasticparts. In [14] the authors studied experimentally the energy efficiency of different SPS devices. The experimental results showed that there is a direct relationship between the densification of the sample and its dimensions. The authors indicated that the maximum temperature occurs at the lateral surface of the sample in the contact surface with

the graphite and that it has an essential effect on the processes of densification and grains coarsening. In [15] the authors investigated experimentally the role of electric current pulses on responsiveness (reactivity) in an SPS device that uses a sample of molybdenum silicide (Mo-Si) (which has a layered crystal structure) instead of a powder sample (solid of polycrystalline structure). They investigated reactivity in the layered structures of molybdenum silicide, with the aim of providing direct quantitative evidence for the role of pulsation. They found that the interaction between the preceding elements resulted in the formation of a product consisting mainly of a major layer of molybdenum disilicide ($MoSi_2$) and a minor layer of molybdenum silicide (Mo_5Si_3). Moreover, they concluded that the direction of the current had no effect on the thickness of the product layer and that the growth rate of the product did not depend on the pulse pattern. In [16] the authors examined the mechanical properties of SPS-sintered composites (316L-TiB2 steel) and their performance at high temperatures. They concluded that the ideal manufacturing temperature for this composite is 1100°C. Additionally, the sintering time plays a crucial role, influencing the component reaction and microstructure homogeneity. In [17] the authors examined the SPS process to understand its different parameters. They found that pressure has a large effect on the destruction of agglomerates, and the resistance between two particles depends on their geometry. In addition, finding optimal parameters for the SPS process is the key to obtaining solid sintered products. In [18] the authors studied the phase composition, structure, properties and decomposition mechanism of $AlMgB_{14}$ based materials by SPS. They found that increasing the heating rate and sintering temperature leads to a decrease in physical and mechanical properties due to the formation of a large number of impurities and single pores. In [19] the authors summarised the work of nearly a decade of research into spark plasma sintering (SPS). They found that pressure-induced atomic-scale defects can play an important role in many physical properties of ceramic materials and in their stability during post-sintering thermal exposure. In [20] the authors evaluated-experimentally the effect of current on the generation of temperature gradients in the radial and axial directions in the sample. The experiment was carried out on two types of samples (alumina and copper). They revealed that the presence of radial and/or axial temperature gradients in the sample could produce inhomogeneities in its chemical composition, in its microstructure and in its green density. Other relevant experimental and/or numerical studies which deal with SPS and related field and which are mainly devoted to the study of the above thermoelectric and mechanical coupling behavior in various SPS devices can be found in the references [21–32].

All the numerical and/or experimental studies above have shown that numerical modeling is particularly relevant for determining the distribution of each of the above fields and in particular the behavior of the thermoelectric and mechanical coupling. This advantage in favor of numerical simulation certainly leads to overcoming all kinds of difficulties encountered in experimental studies, which are particularly expensive, long, complex and difficult to carry out. In this work,

a 3D model to describe the behavior of thermoelectric and mechanical coupling during the SPS process of a polycrystalline material was presented. The model is applied to model the densification (SPS process) of both metal (copper) and ceramic (alumina) samples. The governing equations of the SPS densification model and the thermophysical and mechanical properties of the sample (powder) were incorporated and solved using the ANSYS code [33] in order to numerically analyze the *effects* of the intensity of the electric current and applied uniaxial pressure on the behavior of thermoelectric (electric current density, temperature and heat flux distributions) and mechanical (stress-strain and displacement fields) coupling. This study is motivated, on the one hand, by the lack of 3D numerical simulations that can lead to more or less realistic and precise numerical results. On the other hand, the exact determination of the required applied pressure and the required applied current will greatly help us to *optimize* the *operating* conditions of the SPS device in order to further improve the product quality (densified solid with better microstructure).

2. General considerations and mathematical model

2.1. Description of the SPS device and its geometric characteristics

The system configuration (SPS device) studied here and presented in Fig. 1 was chosen on the basis of models of SPS devices existing in practice and which have been extensively studied in previous experimental and/or numerical work, for example in references [1, 5, 6, 8, 10, 15, 21, 29, 30]. In this configuration, the
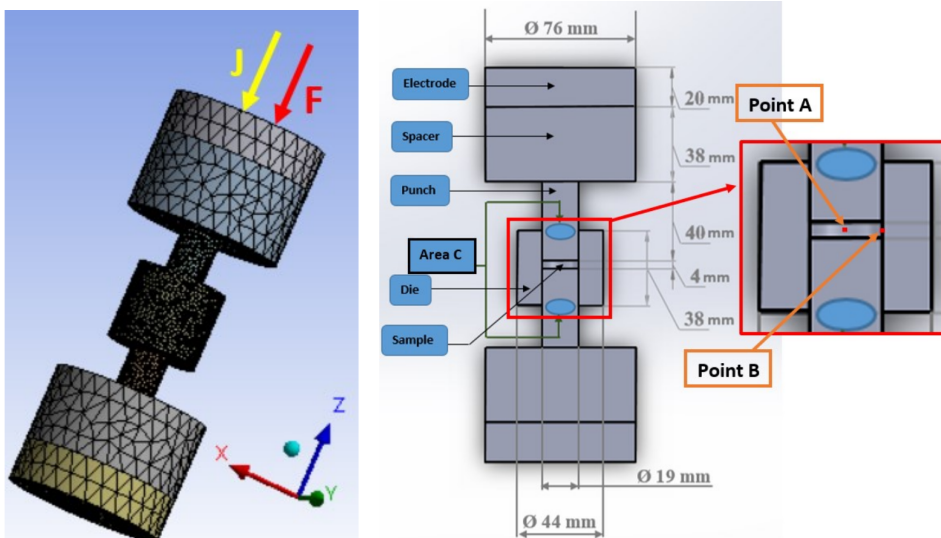
(a) Normal (3D) view with mesh illustration

(b) Cross-sectional view with geometrical characteristics
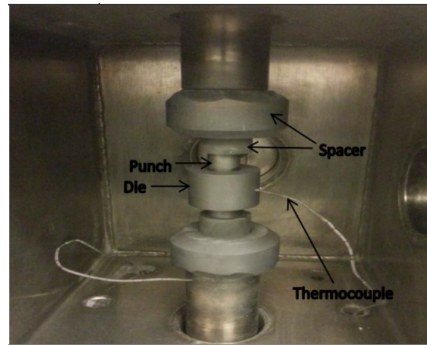
(c) SPS device model 10-3 manufactured by Thermal Technologies LLC
(Santa Rosa, CA, USA). The photo is taken from the reference [34]

Fig. 1. Schematic representation of the studied SPS device (machine): Referring to the reference
frame (X, Y, Z) represented here, the point "A" is taken in the middle of the sample: so its
coordinates are ($X_A = Y_A = 0$ mm); while point B is placed at the edge of the sample and has
coordinates ($X_B = 9.5$ mm and $Y_B = 0$ mm)

sample (copper or alumina) is placed inside a graphite die, and the system mainly
consists of two cylindrical graphite punches, located at the top and bottom of the
sample and each protected by a spacer, and two electrodes which are placed at the
upper and lower ends of the system. The dimensions (geometric characteristics) of
the system are shown in Fig. 1; while the thermophysical and mechanical properties
of all materials used are given in Table 1 [34].

Table 1. Properties of materials [35]

Property	Graphite	Alumina	Copper
Young's modulus, E [MPa]	$2.5 \cdot 10^4$	$3.245 \cdot 10^5$	$1.2962 \cdot 10^5$
Poisson's ratio, ν	0.22	0.24372	0.34496
Bulk modulus, K [MPa]	$1.4881 \cdot 10^4$	$2.1103 \cdot 10^4$	$1.3934 \cdot 10^4$
Shear modulus, G [MPa]	$1.0246 \cdot 10^4$	$1.3046 \cdot 10^5$	$4.8187 \cdot 10^4$
Tensile yield strength, σ_{yT} [MPa]	$1.1 \cdot 10^2$	$3.12 \cdot 10^2$	$2 \cdot 10^2$
Compressive yield strength, σ_{yC} [MPa]	$3.5 \cdot 10^2$	$3.34 \cdot 10^3$	$3 \cdot 10^2$
Density, ρ [kg m^{-3}]	2229.8	3692.8	8940
Specific heat, C_p [J kg^{-1}K^{-1}]	$-398.17 + 4.58T$ $-3.52 \cdot 10^{-3}T^2$ $+1.28 \cdot 10^{-6}T^3$ $-1.82 \cdot 10^{-10}T^4$	$-126.53 + 8.19T$ $-6.1 \cdot 10^{-3}T^2$ $+2.31 \cdot 10^{-6}T^3$ $-3.42 \cdot 10^{-10}T^4$	$355.3 + 0.1T$
Thermal conductivity, k [W m^{-1}K^{-1}]	$90 - 9.54 \cdot 10^{-2}T$ $+8.16 \cdot 10^{-5}T^2$ $-3.2 \cdot 10^{-8}T^3$ $+4.77 \cdot 10^{-12}T^4$	$76.44 - 0.189T$ $+1.959 \cdot 10^{-4}T^2$ $-8.94 \cdot 10^{-8}T^3$ $+1.49 \cdot 10^{-11}T^4$	$420.66 - 0.07T$
Thermal expansion coefficient, α [K^{-1}]	$1.6062 \cdot 10^{-6}$	$7.2255 \cdot 10^{-6}$	$1.7341 \cdot 10^{-6}$
Electric resistivity, ρ_{el} [Ωm]	$3.47 \cdot 10^{-7}$	$1 \cdot 10^{14}$	$2 \cdot 10^{-8}$

In the above device a *pulsed* direct current with an intensity of 1000 A is passed through the graphite punch-die assembly which contains the powder (sample) in order to heat it and at the same time a *uniaxial* pressure of an amplitude of 8.72 MPa is applied to the **upper** electrode of the system (device). The simultaneous application of pulsed current and uniaxial pressure offers the possibility for the SPS technique to obtain very dense samples in a shorter time compared to those obtained by traditional sintering methods. The previous values of pulsating direct current and uniaxial pressure were chosen on the basis of experimental work carried out previously [6].

2.2. Governing equations

The mathematical model presented below is devoted to model the behavior of the thermoelectric and mechanical coupling in the SPS device during the SPS process of a sample (polycrystalline material). In order to simplify the present analysis, the following hypotheses [1, 6, 29, 30] have been made in the model:

2.2.1. Simplifying assumptions

The sample is assumed to be a fully dense material, all materials used are considered to be homogeneous and isotropic materials, only the *small linear elastic* deformation (strain/displacement) was considered and the mechanical behavior is assumed to be quasi-static. Moreover, the heat transfers by radiation and convection are neglected and transient conduction heat transfer is assumed. Finally, no external inward current flow and no external current source are considered. Given these assumptions, the equations governing the thermoelectric and mechanical behavior can be written as following:

2.2.2. Mechanical behavior equations

Mechanical equilibrium equation

Under the assumption that only small linear **elastic** deformation (displacement/strain) is considered, the mechanical equilibrium of the system is governed by the following equation:

$$-\nabla \{\boldsymbol{\sigma}\} = \vec{\mathbf{F}},\tag{1}$$

where $\{\boldsymbol{\sigma}\}$ is the stress tensor and $\vec{\mathbf{F}}$ is the applied load.

As the mechanical behavior is assumed to be elastic, Hooke's law is written

$$\{\boldsymbol{\sigma}\} = [\mathbf{D}]\{\boldsymbol{\varepsilon}\},\tag{2}$$

where $[\mathbf{D}]$ is elasticity matrix and $\{\boldsymbol{\varepsilon}\}$ is the elastic strain tensor.

On the other hand, the strain tensor due to thermal expansion α for an isotropic material is given by:

$$\{\boldsymbol{\varepsilon}^{\text{th}}\} = \alpha \left(T - T_{\text{ref}}\right) \{\boldsymbol{\delta}\},\tag{3}$$

where $\{\delta\}$ is the Kronecker tensor (identity matrix), T is the temperature, T_{ref} is taken as the reference temperature (at the reference state) of the system, and α is the coefficient of thermal expansion.

Taking into account the thermal coupling, the **overall** stress tensor is written as

$$\{\sigma\} = [\mathbf{D}] \left\{\varepsilon + \varepsilon^{\text{th}}\right\}. \tag{4}$$

Recall that in the global coordinate system (coordinates of the fixed Cartesian frame, see Fig. 1), the elastic and thermal strains are expressed respectively by:

$$\{\varepsilon\} = \begin{bmatrix} \varepsilon_X & \varepsilon_{XY} & \varepsilon_{ZX} \\ \varepsilon_{XY} & \varepsilon_Y & \varepsilon_{YZ} \\ \varepsilon_{ZX} & \varepsilon_{YZ} & \varepsilon_Z \end{bmatrix}, \tag{5}$$

where

$$\varepsilon_X = \partial U/\partial X,$$
$$\varepsilon_Y = \partial V/\partial Y,$$
$$\varepsilon_Z = \partial W/\partial Z,$$
$$\varepsilon_{XY} = \frac{1}{2}\left(\partial U/\partial Y + \partial V/\partial X\right),$$
$$\varepsilon_{YZ} = \frac{1}{2}\left(\partial V/\partial Z + \partial W/\partial Y\right),$$
$$\varepsilon_{ZX} = \frac{1}{2}\left(\partial W/\partial X + \partial U/\partial Z\right),$$

and

$$\{\varepsilon^{\text{th}}\} = \alpha\,(T - T_{\text{ref}})\,\{\delta\} = \begin{bmatrix} \alpha\,(T - T_{\text{ref}}) & 0 & 0 \\ 0 & \alpha\,(T - T_{\text{ref}}) & 0 \\ 0 & 0 & \alpha\,(T - T_{\text{ref}}) \end{bmatrix}. \tag{6}$$

In addition, the mechanical displacement vector ($\vec{\mathbf{U}}$) and the elastic matrix $[\mathbf{D}]$ (for the isotropic material) are given respectively by:

$$\vec{\mathbf{U}} = \begin{pmatrix} U \\ V \\ W \end{pmatrix} \tag{7}$$

and

$$[\mathbf{D}] = \begin{bmatrix} \lambda + 2\mu & \lambda & \lambda & 0 & 0 & 0 \\ \lambda & \lambda + 2\mu & \lambda & 0 & 0 & 0 \\ \lambda & \lambda & \lambda + 2\mu & 0 & 0 & 0 \\ 0 & 0 & 0 & \mu & 0 & 0 \\ 0 & 0 & 0 & 0 & \mu & 0 \\ 0 & 0 & 0 & 0 & 0 & \mu \end{bmatrix}. \tag{8}$$

Or

$$[\mathbf{D}] = \frac{E}{(1+v)(1-2v)}\begin{bmatrix} 1-v & v & v & 0 & 0 & 0 \\ v & 1-v & v & 0 & 0 & 0 \\ v & v & 1-v & 0 & 0 & 0 \\ 0 & 0 & 0 & \frac{1-2v}{2} & 0 & 0 \\ 0 & 0 & 0 & 0 & \frac{1-2v}{2} & 0 \\ 0 & 0 & 0 & 0 & 0 & \frac{1-2v}{2} \end{bmatrix},$$

where λ and μ are the Lamé's parameters given respectively by:

$$\lambda = \frac{Ev}{(1+v)(1-2v)} \quad \text{and} \quad \mu = \frac{E}{2(1+v)}.$$

2.2.3. Thermoelectric behavior equations

Continuity equation (electrical charge balance)
From Maxwell's equations, the electric direct current flow in the system can be written [36]:

$$\boldsymbol{\nabla}\vec{\mathbf{J}} = 0, \tag{9}$$

where the electric current density, $\vec{\mathbf{J}}$, is given by Ohm's law:

$$\vec{\mathbf{J}} = \sigma_{el}\vec{\mathbf{E}} + \vec{\mathbf{J}}_e , \tag{10}$$

where σ_{el} is the electrical conductivity, $\vec{\mathbf{J}}_e$ is the generated external current density (taken neglected in the present analysis as indicated previously) and $\vec{\mathbf{E}}$ is the electric field which is given by

$$\vec{\mathbf{E}} = -\boldsymbol{\nabla}\varphi, \tag{11}$$

where φ is the electric potential.

By combining the above equations, we can rewrite equation (8) (expressing the electrical charge balance) as follows:

$$\boldsymbol{\nabla}\vec{\mathbf{J}} = \boldsymbol{\nabla}\left(\sigma_{el}\vec{\mathbf{E}}\right) = \boldsymbol{\nabla}\left(-\sigma_{el}\boldsymbol{\nabla}\varphi\right) = 0. \tag{12}$$

Thus, the equation for the conservation of **electric potential** is given by

$$\boldsymbol{\nabla}\left(-\sigma_{el}\boldsymbol{\nabla}\varphi\right) = 0. \tag{13}$$

Heat transport equation
Transient heat transport by conduction in the system is given by:

$$\rho C_p \frac{\partial T}{\partial t} - \boldsymbol{\nabla}\left(k\boldsymbol{\nabla}T\right) = Q, \tag{14}$$

where $-k\boldsymbol{\nabla}T$ is the heat flux (conductive heat flux), T is the temperature, k, ρ and C_p are, respectively, the thermal conductivity, the density and the heat capacity of the system and Q is the heat generated (by Joule effect) per unit volume due to current flow in the system. The last volumetric heat source can be expressed using Joule's law as follows:

$$Q = \vec{\mathbf{J}}.\vec{\mathbf{E}} = J\,E. \tag{15}$$

2.2.4. Initial and boundary conditions

The above system of partial differential equations can be solved if the initial and the corresponding well-posed boundary conditions are defined. Before starting the process at the time $t = 0$ s, the following initial conditions are applied: the initial electrical potential is set to zero, the initial temperature of the whole system is assumed equal to the ambient temperature and taken equal to 300 K, and the stress-strain fields are initially zero [6].

On the other hand, the system is subject to the following boundary conditions (these boundary conditions are similar to those used in the experimental work [6]):

Electric potential boundary conditions

– Although the method of applying current varies from laboratory to laboratory (direct current, pulsed direct current at variable frequency), it is worth noting that the application of direct current (DC) in the finite element model precisely approximates the pulsed current involved in real SPS experiments [6, 9, 12, 13]. In our study, electrical energy is supplied by applying a voltage difference between the electrodes (the electrical potential in the top surface of the electrode is coupled (with a value of 1 V), as well as in the surface at $z = 0$ (with a value of $V = 0$)). There is therefore an electrical potential difference $DV = 1$ V across the ends of the geometry studied [12, 13, 20] and, in this way, a current flows through the whole assembly, from the upper electrode to the lower electrode, supplying the device with an electrical current of maximum value $I = 1000$ A for 600 s (controlled by the software). The power supply is then put off at time 600 s [12, 20]. All other external surfaces of the system (SPS device) are assumed to be electrically insulated.

Thermal boundary conditions

– In spark plasma sintering, the thermal and electrical contact resistances have given rise to a debate between different researchers. Indeed, the first group of researchers argued that consideration of contact resistance is key to gaining a more accurate understanding of temperature and electric current density distributions [1, 5, 7, 10, 37] in the SPS system, particularly in the punch-die-sample assembly. Unlike the first group, another group of researchers felt that contact resistances can be ignored due to their inverse relationship with applied temperature and pressure [2, 6, 12, 13, 16, 19]. They argue that these resistances exhibit secondary effects at high temperatures and pressures, and this holds true for SPS as well. Moreover, the contact resistances depend on the surface condition of the components [19], which makes an exact estimation of these resistances a very delicate

task. The second group of researchers was supported by alternative experiments, carried out on different SPS processes. Indeed, in some experiments researchers used a sheet of graphite to fill the contact interfaces, aiming to minimize the impacts of electrical and thermal contact resistances [9, 33, 34]. Other researchers have also claimed that contact resistances can be neglected by implementing measures such as reducing heat loss from the die through thermal insulation and using a non-conductive coating on its outer surface. They also suggest decreasing the resistance at the die-punch interface by preventing the entrapment of powder particles: by ensuring a smooth surface (where the punch and the die come into contact) or by using a highly conductive coating [11]. Moreover, it should be pointed out that the inclusion of contact resistances in the SPS requires specific measurements for each experiment and sintering machine [19]. For all these reasons, the effect of contact resistances has been neglected in the present study.

– **On all external surfaces**, heat loss by radiation was taken into acount in this work by: $f = v\varepsilon(T_w^4 - T_0^4)$ where f is the heat flux per unit area; v is the emissivity, wich is assumed equal to 0.8; ε is the Stefan-Boltzmann constant; $\varepsilon = 5.6704 \cdot 10^{-8}$ W/m^{2}K^4; T_w is the temperature of the surface; and T_0 is the ambient temperature [2, 5, 13, 20].

– **On all external vertical surfaces,** the heat transfer by convection of all the external surfaces of the SPS device is taken into account (due to the direct contact of these surfaces with the air). A heat transfer coefficient, h, is estimated here equal to 5 W m^{-2}K^{-1}. (We opted for a reduced value of the heat transfer coefficient, as the chamber is considered to be under vacuum in some studies. Nevertheless, we have not neglected this phenomenon, as it has a significant impact at high temperatures.)

– On the upper and lower surfaces of the electrode the temperature is set to be 300 K [6].

Mechanical equilibrium boundary conditions

– All external surfaces of the system are considered as free (unloaded) surfaces (i.e., there is no support or force applied) except on the upper end of the upper electrode which is subjected to pressure and the lower end of the lower electrode which is considered a *fixed support*. In other words, the upper electrode is subjected to auniaxial pressure equal to 8.72 MPa [6]; whereas, the underside of the lower electrode is *fixed* (the electrode is placed on the ground).

– The friction, between the sample and the walls of the die and the two upper and lower punches, is neglected in this work in order to simplify the simulation. Moreover, the friction between all the other remaining contact surfaces of the device is neglected. This assumption can be justified by the fact that the applied force is perpendicular to almost all the contact surfaces (i.e., the horizontal contact surfaces which are in the majority). Also, this hypothesis can be justified by referring to the experiments carried out in [9, 37, 38].

3. Numerical resolution procedure and model validation

3.1. Mesh sensitivity study

It is well known that the choice of the mesh is an essential stage in the procedure of numerical resolution of the problem and the good choice will be that which makes it possible to have convergent and precise results with a minimum of cost of calculation; it is therefore necessary to calculate the different fields (mainly temperature, electric current density, stress-strain, displacement) of the problem studied at a given point inside the system using different mesh resolutions and to compare the results obtained between them. By taking for example points A and B, randomly chosen in the system (see Fig. 1), and performing the calculation using the following mesh resolutions: the first mesh "Mesh (1)" consists of 108950 nodes and 73873 elements, the second mesh "Mesh (2)" is composed of 128305 nodes and 87342 elements, and the third mesh "Mesh (3)" is composed of 150583 nodes and 102890 elements, one can obtain the results presented in Table 2. Note that: in the three cases of meshing, the meshing was carried out in such a way that the finest meshing section is located in the punch-die-sample assembly (Fig. 1) and the calculation was carried out on a personal computer which has the characteristics (an i5 processor and a 8GB RAM).

Table 2. Results obtained from the different meshes

Quantity	Sample	Mesh (1)	Mesh (2)	Mesh (3)	Maximum relative error
von Mises stress (at Point A), σ_{eA} [MPa]	alumina	193.07	195.97	195.5	1.47%
	copper	98.433	99.126	98.578	0.69%
Equivalent strain (at Point A), ε_{eA}	alumina	$5.951 \cdot 10^{-4}$	$6.0396 \cdot 10^{-4}$	$6.0258 \cdot 10^{-4}$	1.46%
	copper	$7.5943 \cdot 10^{-4}$	$7.6476 \cdot 10^{-4}$	$7.6063 \cdot 10^{-4}$	0.69%
Displacement in X-direction (at Point A), U_A [mm]	alumina	$-2.6337 \cdot 10^{-4}$	$-2.6275 \cdot 10^{-4}$	$-2.6348 \cdot 10^{-4}$	0.27%
	copper	$-2.6025 \cdot 10^{-4}$	$-2.6132 \cdot 10^{-4}$	$-2.6195 \cdot 10^{-4}$	0.64%
Temperature (at Point A), T_A [K]	alumina	1060.9	1061.9	1062.8	0.17%
	copper	1050.3	1051.3	1052.2	0.18%
Heat flux (at Point B), q_B [W m^{-2}]	alumina	94.346	93.88	94	0.49%
	copper	929.80	915.07	954.27	4.10%
Current density (at Point A), J_A [A m^{-2}]	alumina	$1.2992 \cdot 10^{-14}$	$1.3126 \cdot 10^{-14}$	$1.3046 \cdot 10^{-14}$	1.02%
	copper	$1.0263 \cdot 10^{6}$	$1.023 \cdot 10^{6}$	$1.022 \cdot 10^{6}$	0.41%
Computational cost		About 5.5 hours of CPU time	About 6 hours of CPU time	About 6.5 hours of CPU time	

The comparison between the results presented in Table 2 shows that there is a slight difference between the results obtained from the three types of mesh resolution (a small relative error between the maximum value and the minimum value obtained by each mesh case). One can then judge useful to choose the second mesh (Mesh 2) in all the calculations carried out thereafter. This choice will allow us to obtain more accurate results in a relatively reduced computation time.

3.2. Model validation and confrontation with other models

As mentioned before, the authors of reference [6] carried out an experimental study as well as a numerical one to study an SPS device similar to that shown in Fig. 1; but their numerical model was two-dimensional (2D) and in which the authors also neglected the effect of heat exchanges by convection at the level of the **external** surfaces of the SPS device since these are exposed to the air; these simplifications are unrealistic and may lead to inaccuracies in the predicted numerical results. Instead and to remedy these shortcomings, we have carried out in this work a 3D numerical study in which we have taken into account the convection effect, which allows us to carry out a more realistic and more precise simulation.

The present simulation uses the same experimental/numerical data performed previously in [6]; namely: an electric current of intensity "1000 A" and a uniaxial mechanical pressure of magnitude "8.72 MPa" applied to the system (SPS device) during the interval from $t = 0$ s to $t = 600$ s and the results simulation and comparison are presented in Figs. 2 and 3.
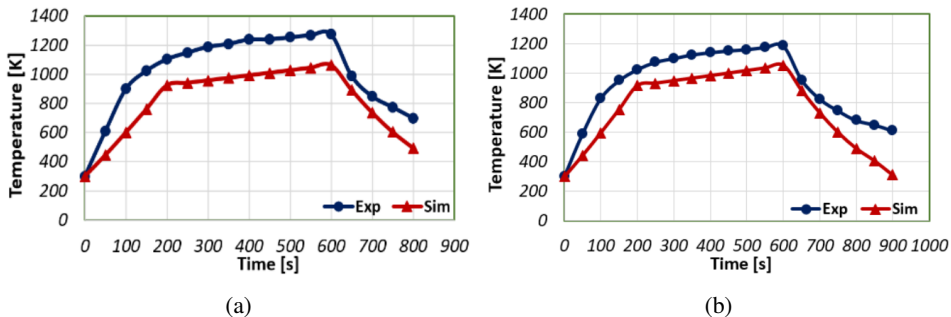

Fig. 2. Time evolutions of temperature at point "A" during the sintering interval for (a) alumina and (b) copper. Comparison between present numerical results and experimental results in [6, 12]

Fig. 2 shows the temperature evolutions at point "A" in Fig. 1 during the sintering time of the two samples of alumina and copper, respectively. These evolutions have been measured experimentally in [6, 12] and calculated numerically in this analysis. It should be noted that the experimental results made in [6] and [12] are almost similar. The comparison between the numerical results and the experimental results shows an acceptable agreement. Indeed, the maximum difference between the measured value and the calculated one does not exceed 35% for the two cases

of the sample. This difference is mainly attributed to the inaccuracy of the values of the thermophysical properties of the materials that were used in the present calculations.

Likewise, Fig. 3 shows the variations of *axial* stress (σ_z) in the *radial* direction (r) (starting from point "A" towards the die wall) during SPS sintering of the alumina sample. Stress values were measured in [6] and calculated here, respectively. In this case, one can observe a difference between the present numerical results and the experimental measurements. This difference has been well *underlined* in a multitude of previous experimental and/or numerical works as shown in Table 3. In fact, the difference in the above results can be attributed to several factors such as the imprecision of the mechanical properties of the materials that are used in the calculations, and the sample size (see Table 3). Indeed, in the experiments and/or numerical studies cited above, the mechanical properties of the materials and the size of the sample (which were used by the authors) have values close to but not necessarily identical to those chosen here (see Tables 3 and 4).

Table 3. Maximum values of stresses predicted and/or measured (at points "A" and "B" in Fig. 1) in various previous studies

Reference	Sample	Radial stress*, σ_r [MPa]		Axial stress, σ_z [MPa]		Hydrostatic stress**, σ_{hyd} [MPa]	
		Point A	Point B	Point A	Point B	Point A	Point B
Present simulation	alumina	$\sigma_r = 315$	$\sigma_r = 149$	$\sigma_z = 119$	$\sigma_z = 106$	250	135
	copper	$\sigma_r = 38$	$\sigma_r = 7$	$\sigma_z = 60$	$\sigma_z = 102$	45	39
[6]	alumina	–	–	–	–	–	–
	copper	$\sigma_r \approx 72$	–	$\sigma_z \approx 144$	–	–	–
[12]	alumina	–	–	–	–	70	32
	copper	–	–	–		330	355
[39]	copper	–	–	–		Maximum principal stress in the sample = 360	
[40]	copper	–	–	–		Maximum principal stress in the sample = 365	
[1]	alumina	–	–	51	58	–	–
[38]	zirconium	$\sigma_r = 600$	$\sigma_r = 500$	100	100	–	–
[41]	Alpha alumina	$(\sigma_r)_{max} = 45$		$(\sigma_z)_{max} = 60$		–	–

* Recall that σ_r and σ_z are respectively the radial and axial stress components in the cylindrical coordinate system (r, θ, z)

** The hydrostatic stress is the average of the three principal stresses (σ_1, σ_2 and σ_3) and given by $\sigma_{hyd} = \dfrac{\sigma_1 + \sigma_2 + \sigma_3}{3}$.

Three-dimensional numerical study of the behavior of thermoelectric and mechanical. . .   511
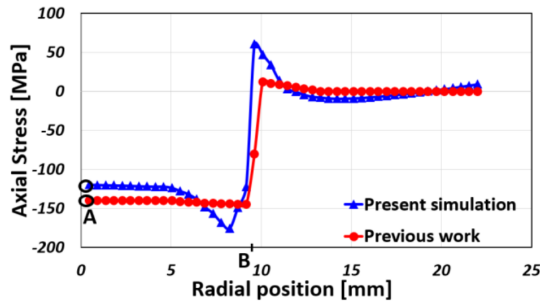

Fig. 3. Variations of the "normal" axial stress (σ_z) in the radial direction (r) (starting from point "A" towards the die wall) during the sintering of the alumina sample. As shown, a difference can be observed between the current numerical results and the experimental measurements, in particular at the level of the sample/die interface (Point B of Fig. 1). With the exception of the region of the sample/die interface, an acceptable agreement can be observed between the calculated stress values and those measured experimentally in [6]

Table 4. Values of applied pressures and mechanical properties and sample sizes used in this simulation and in various previous studies

Reference	Sample	Applied pressure, p [MPa]	Sample size (D, H) [mm]	Young's modulus, E [GPa]	Poisson's ratio
Present simulation	alumina	8.72	D = 19, H = 4	324.5	0.24
	copper	8.72	D = 19, H = 4	129.6	0.34
[6]	alumina	8.72	D = 19, H = 4	–	–
	copper	8.72	D = 19, H = 4	–	–
[12]	alumina	1.016	D = 19, H = 3	215	0.32
	copper	1.016	D = 19, H = 3	110	0.33
[39]	copper	50	D = 20, H = 5	-	-
[40]	copper	8	Dog-bone	-	-
[1]	alumina	3.125	D = 20, H = 4	300	0.22
[38]	zirconium	100	D = 20, H = 5	383	0.18
[41]	Alpha alumina	20	D = 20, H = 5	$400 \cdot [1 - 86.6 \cdot 10^{-6}(T - 273)$ $-40.7 \cdot 10^{-9}(T - 273)^2$ $+8.7 \cdot 10^{-2}(T - 273)^3]$	0.23

4. Results and discussion

4.1. Mechanical behavior of the punch-die-sample assembly during SPS process

4.1.1. Mechanical stresses distributions

Von Mises and shear-stresses distributions

Fig. 4a and 4b show the "equivalent" von Mises stress (σ_e) distributions in the SPS device, calculated respectively for the cases of sintering copper and alumina

samples at $t = 600$ s (i.e., at the end of the sintering time). For the case of the copper sample, the maximum stress is located at the wall of the punch near the spacer; while in the case of the alumina sample, the maximum stress is located in the area close to the edge of the punch-die-sample assembly and its value is greater than that calculated for the first case. Moreover, Fig. 4c and 4d show the *shear* stress (τ_{XY}) distributions calculated, respectively, for the copper and alumina samples at $t = 600$ s. For the case of the copper sample, the significant shear-stress is observed in the punch-die-sample contact surfaces and in the wall of the punch where it shows high values in these regions but it shows low values in the rest of the system. However, in the case of the alumina sample, the critical shear-stress zone is located in the die-sample contact surface and we further notice that in general the whole system is subjected to small values shear-stress compared to von Mises stresses.

Cross-sectional view 3D view   Cross-sectional view 3D view
(a) Von Mises stress (copper sample)   (b) Von Mises stress (alumina sample)

(c) shear-stress (copper sample)   (d) shear-stress (alumina sample)
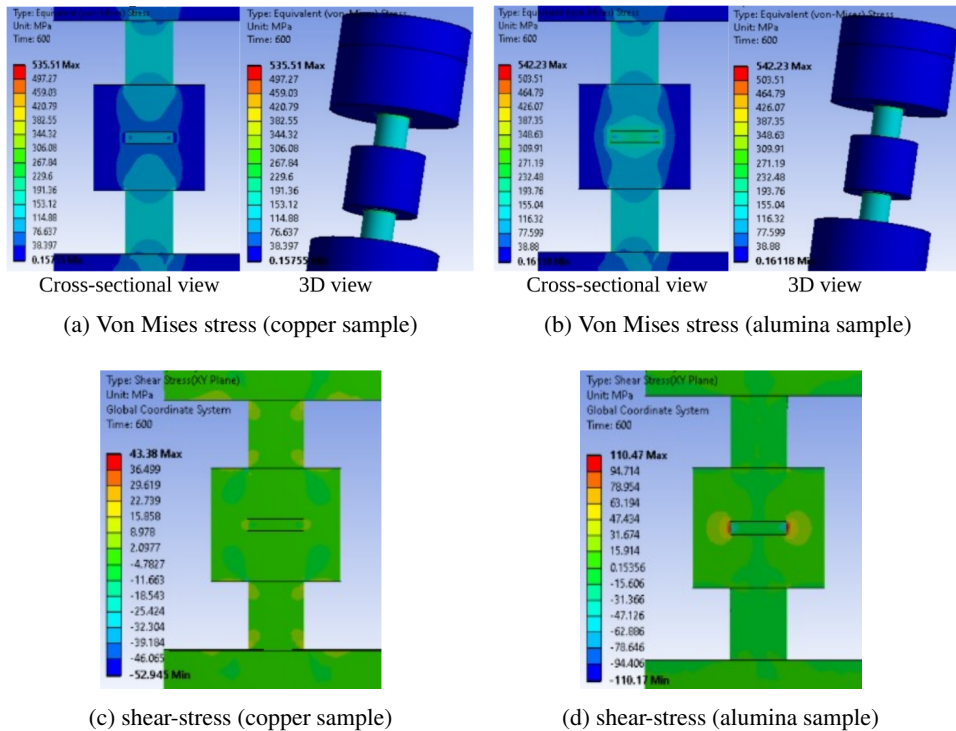
Fig. 4. Distributions of von Mises and shear-stresses in the SPS device, calculated respectively for the copper and alumina samples at the sintering time $t = 600$ s

In this representation and all subsequent representations, special emphasis is placed on the punch-die-sample assembly area. Note that the effective and shear-stresses (σ_e and τ_{XY}) are presented in the frame of reference shown in Fig. 1.

Likewise, Fig. 5c and 5d show the normal-stress in X-direction (σ_X) distributions in the SPS device calculated for the copper and alumina sample cases, respectively. For the case of the copper sample, the normal-stress (σ_X) has rel-

atively low values in the sample and high values in the punch with a maximum in the spacer-punch contact area. Whereas for the alumina sample, the critical normal-stress (σ_X) zone is observed at the surface of the sample which is in contact with the die; moreover, there are large values for the axial stress in the punch. Therefore, on the one hand, the area where the maximum cross-sectional variation is found is the most critical area and this is where the maximum normal-stress for copper is found. While the maximum value of the radial stress for alumina is in the die-sample contact zone. On the other hand, the normal-stress (σ_X) decreases uniformly in the die (from the center towards the walls) with an increasing radius in both cases.

(a) Normal stress in Z-direction (σ_Z) (copper sample)

(b) Normal stress in Z-direction (σ_Z) (alumina sample)

(c) Normal stress in X-direction (σ_X) (copper sample)

(d) Normal stress in X-direction (σ_X) (alumina sample)
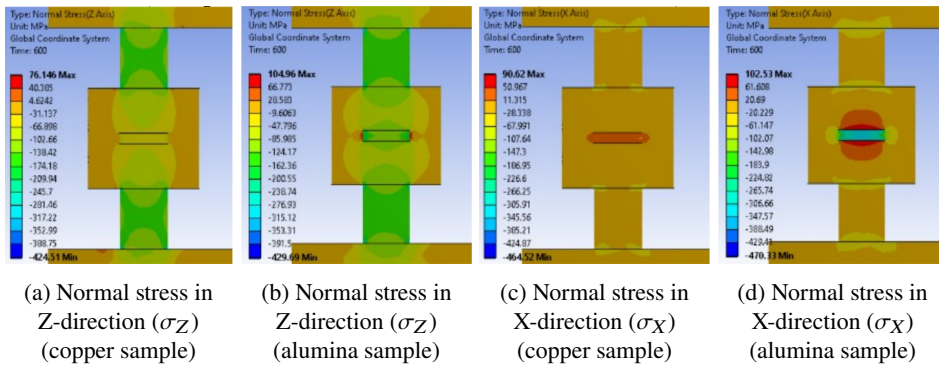
Fig. 5. Distributions of normal-stress components (in the X and Z-directions) in the punch-die-sample assembly calculated respectively for copper and alumina samples at 600 s. The normal-stress components are predicted in the reference frame (X, Y, Z) shown in Fig. 1. The present results also show that the distributions (σ_Y) are almost similar to (σ_X)

Finally, a comparison between Fig. 5a and 5c and Fig. 5b and 5d shows that the maximum value of σ_X stress component is almost twice as much as the maximum value of σ_Z stress component in copper sample; whereas, the σ_X stresses in the alumina are low compared to the σ_Z stresses. This paradox is essentially the result of two parameters (criteria), namely the coefficient of thermal expansion and the Poisson's ratio, which are those which allow the σ_Z stresses to develop freely in alumina unlike copper. Indeed, the higher coefficient of thermal expansion in alumina than in copper, the higher Poisson's ratio in copper than in alumina (see Table 1) are mainly responsible for these results.

Normal stresses distributions

On the other hand, Fig. 5a and 5b show the distributions of the *normal*-stress in Z-direction (σ_Z) calculated in the SPS device for the copper and alumina sample cases, respectively. For the case of the copper sample, the maximum normal-stress in Z-direction (σ_Z) is located in the punch-spacer contact zone. Moreover, significant values of the (σ_Z) are observed also in the upper part of the punch-die contact surface located in the zone where the punch meets the die (see zone (C) illustrated in Fig. 1); but the normal-stress (σ_Z) values are relatively low in

the sample because copper has a high Poisson's ratio and a low coefficient of thermal expansion. While in the case of alumina, the values of the normal-stress in Z-direction are high throughout the system compared to the case of the copper sample, especially in the sample itself and in the part of the punch (the part close to the sample); it is in this last zone that it is observed that the values of the radial stress are the highest. In fact, for the two cases of samples (copper and alumina) there is an accumulation of normal-stresses (σ_Z) in the two punches (close to the sample), but this accumulation is limited at the level of the punch-sample contact surface and it narrows along the punch. Moreover, the normal-stress (σ_Z) is not significant in the two samples; this is attributed to the totally different thermomechanical characteristics of the two materials (copper and alumina), in particular the Poisson's ratio (see Table 1).

4.1.2. Mechanical strains distributions

Equivalent elastic and thermal strains distributions

Fig. 6a and 6b show the equivalent elastic strain (ε_e) distributions in the SPS device, predicted respectively for the sintering cases of copper and alumina samples

Cross-sectional view 3D view	Cross-sectional view 3D view
(a) Equivalent strain (copper sample)	(b) Equivalent strain (alumina sample)

(c) Thermal strain in X-direction (copper sample)	(d) Thermal strain in X-direction (alumina sample)
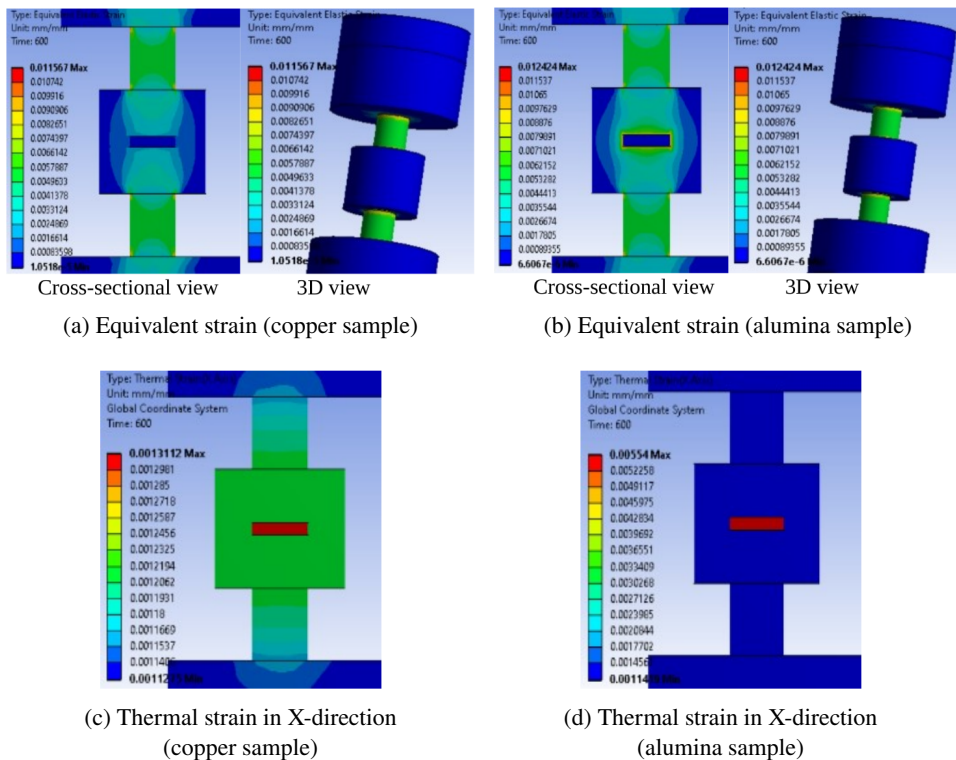
Fig. 6. Distributions of the "equivalent elastic" and "thermal in the horizontal direction" strains in the punch-die-sample assembly calculated respectively for the copper and alumina samples at 600 s

at $t = 600$ s. For the two sampling cases, it can be seen that the equivalent elastic strains are almost similar in the two punches but completely different in the punch-die-sample assembly zone. For the case of the copper sample, it is observed that the strain takes on low values in the punch-die-sample assembly; whereas in the case of the alumina sample, it takes on significant values in all the walls of the sample, in the punch and in the die (the maximum value of equivalent elastic strain is located in the die-sample contact surface).

Moreover, the distributions of the thermal strain component along the horizontal direction (X direction in Fig. 1) (ε_X^{th}) in the two sampling cases (Fig. 6c and 6d) indicate that the coefficient of thermal expansion of the sample plays a crucial role. Indeed, Fig. 6c illustrates that the coefficient of thermal expansion of copper marks its important role in the distribution of the horizontal component of thermal strain and indicates that the sample and the die deform in the same way and with the same values. Whereas, in the case of the alumina sample, the values of the horizontal component of thermal strain are low in the die and the whole system except the sample (see Fig. 6d) where it is observed that its value is greater than the maximum thermal strain value in the case of the copper sample.

Normal elastic strain distributions

Likewise, Fig. 7a and 7b show the normal elastic strain component in X-direction (ε_X) distributions in the SPS device, predicted respectively for the sintering cases of copper and alumina samples at $t = 600$ s. For the copper sample, the maximum strain (ε_X) is in the free wall of the punch and it can be observed that the punch is the most deformed part because it has the small section and this section is the element that makes the difference in this case because the coefficients of thermal expansion of copper and graphite have almost the same value. For the second sample (alumina), it can be seen that the maximum strain value is located in the part of the die which is in direct contact with the alumina. This is due to the Poisson's ratio which is the first criterion allowing the sample to deform in the radial direction and this coefficient (ratio) forces the die to deform in the same
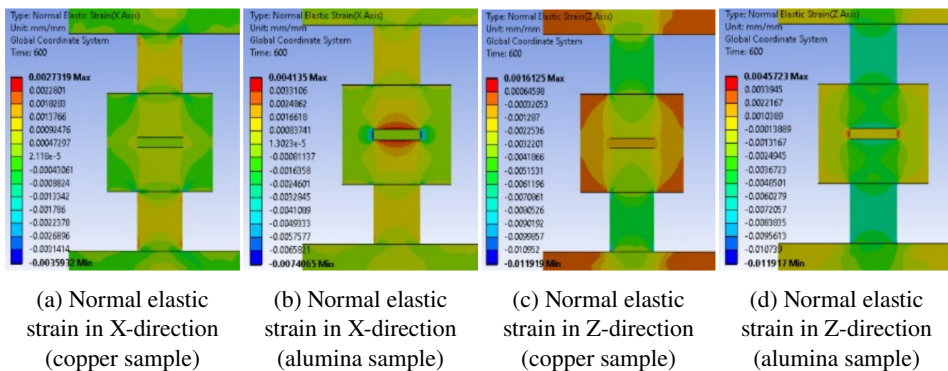

(a) Normal elastic strain in X-direction (copper sample) (b) Normal elastic strain in X-direction (alumina sample) (c) Normal elastic strain in Z-direction (copper sample) (d) Normal elastic strain in Z-direction (alumina sample)

Fig. 7. Distributions of "horizontal" and "vertical" normal elastic strains in the punch-die-sample assembly calculated respectively for the copper and alumina samples at 600 s

direction (in the region close to its contact surface with the sample). In addition, large strains can be noticed in the punch, which start from its contact surface with the sample and they gradually decrease in the axial direction; this trend is due to the deformation of the die and the sample. In fact, when the zone of the die, which is close to the sample and in contact with the punch, is deformed under the effect of the radial deformations of sample, it becomes feeble and allows the punch to deform radially. In addition, Fig. 7c and 7d show the normal elastic strain component in vertical direction (Z-direction in Fig. 1) (ε_Z) distributions in the SPS device, predicted respectively for the sintering cases of copper and alumina samples at 600 s. It can be observed that the strains (ε_Z) in the free parts of the punch, which contain the maximum strain (in the wall of the punch), are almost similar in the two sample cases because the criteria in this case are: the material used in the SPS device (i.e., graphite), boundary conditions and applied pressure; these criteria being the same for the two sample cases. It can also be observed that the strains in the punch-die-sample assembly are different. Indeed, in the case of the copper sample, the large strains are located in the horizontal part of the wall of the die and that they take on small values in the sample; whereas in the case of the alumina sample, the strain takes on significant values in the die-sample contact surface. This difference is due to the difference in the thermal expansion coefficients of the two samples (copper and alumina).

Remark: It should be noted here that the observations and remarks made on the elastic strain distributions are the same as for the elastic stress distributions and this is due to the direct link between stress and strain (Hooke's law).

4.1.3. Mechanical displacements fields

Fig. 8a and 8b show the "horizontal" component of displacement fields (*U*) in the SPS device, predicted respectively for the sintering cases of copper and alumina samples at *t* = 600 s. For the case of the copper sample, the distributions of stresses and strains, discussed previously, will allow the die to have the maximum "horizontal" displacements, which thus forces the sample to have the minimal displacements; this is the explanation of what can be seen in Fig. 8a: "the wall of the die has maximum values of displacements and these displacements decrease uniformly with the radius of the sample (from the end towards the center)". However, in the case of the alumina sample, the maximum "horizontal" displacements are in the die-sample contact zone (most critical deformation zone) with a parabolic shaped extension, which starts from the surface of sample-die contact up to the wall of the die (Fig. 8b). Additionally, Fig. 8c and 8d show the "vertical" displacement fields (*W*) in the SPS device, predicted for the sintering cases of copper and alumina samples respectively at *t* = 600 s. Here, one expects to observe vertical displacements in the direction of the application of load (pressure) in the upper part of the machine (SPS device) and vertical displacements in the direction of the reaction in the lower part of the machine. Indeed, for the two cases of samples,

small vertical displacements can be observed in the direction of the application of the force (pressure).

Cross-sectional view   3D view   Cross-sectional view   3D view
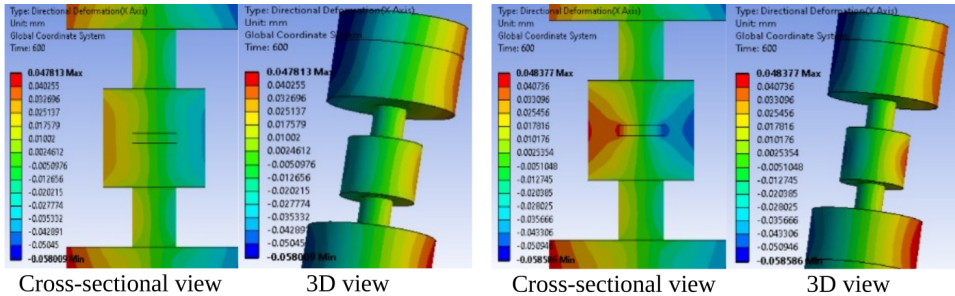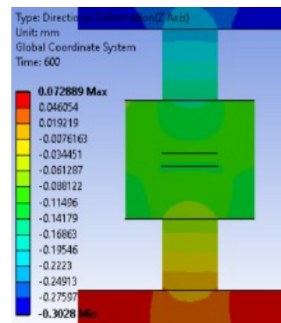
(a) Horizontal displacement (copper sample)   (b) Horizontal displacement (alumina sample)
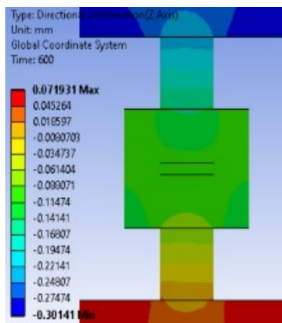
(c) Vertical displacement (copper sample)   (d) Vertical displacement (alumina sample)

Fig. 8. Distributions of directional ("horizontal" and "vertical") displacements in the punch-die-sample assembly calculated respectively for the copper and alumina samples at 600 s

4.2. Thermoelectric coupling in the punch-die-sample assembly during the SPS process

4.2.1. Temperature and heat flux distributions

Figs. 9 to 11 show respectively the distributions of the thermal field and the "total" and "directional" thermal fluxes in the SPS device, predicted respectively for the cases of copper and alumina samples at $t = 600$ s. It can be seen that in the case of the alumina sample the temperature reaches the value of (1061 K); which is higher than the value reached in the case of the copper sample (1051 K) (see Fig. 9a and 9b). This is due to the difference in the electrical resistivities of the two samples. Although the temperature is higher in the case of the alumina sample than in the case of the copper sample, it can however be observed that the total heat flux is greater in the case of the alumina sample (see Fig. 10a and 10b). This is attributed to the difference in the thermal conductivities of the two samples, and to the temperature reached (higher in the case of alumina than in copper). Moreover,

for both samples, it can be observed that the heat flux in the vertical direction (q_Z) is greater than that in the horizontal direction (q_X) (see Fig. 11a and 11c and Fig. 11b and 11d, respectively). This tendency is the direct consequence of
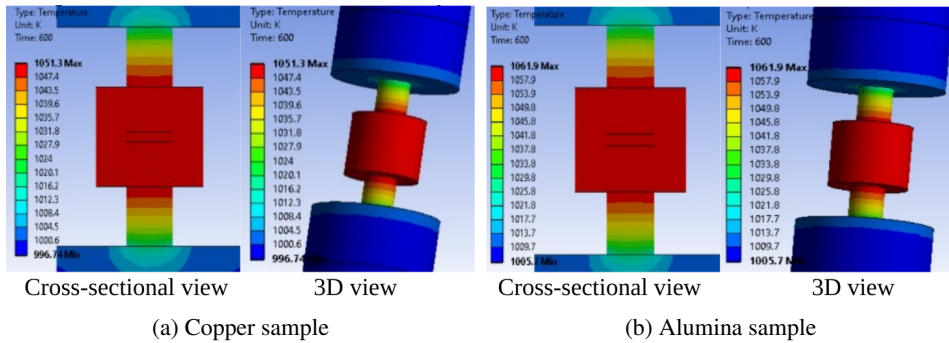

Cross-sectional view   3D view   Cross-sectional view   3D view

(a) Copper sample   (b) Alumina sample

Fig. 9. Temperature distributions in the punch-die-sample assembly, calculated respectively for (a) copper and (b) alumina samples at 600 s

Cross-sectional view   3D view   Cross-sectional view   3D view
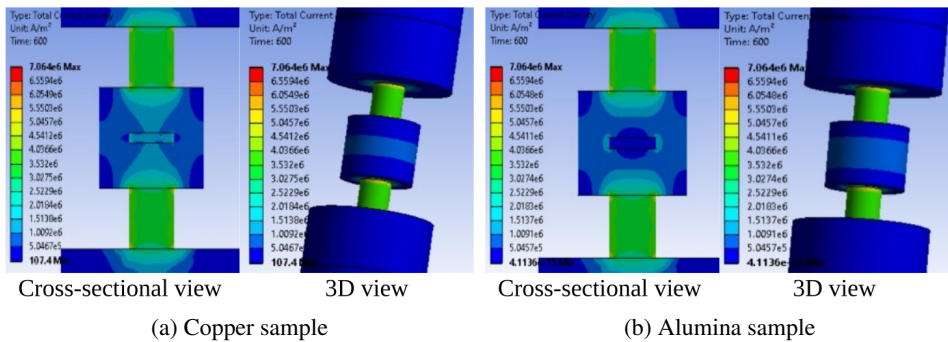
(a) Copper sample   (b) Alumina sample
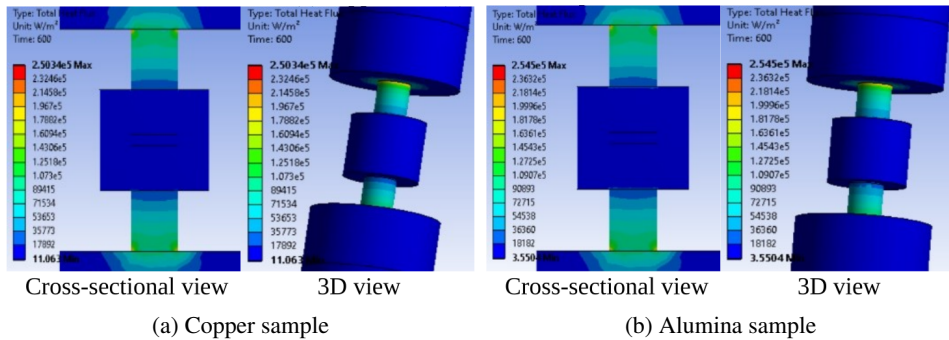
Fig. 10. Distributions of total heat flux in the die-punch-sample assembly calculated respectively for (a) copper and (b) alumina samples at 600 s

(a) Component of heat flux in Z-direction (copper sample)   (b) Component of heat flux in Z-direction (alumina sample)   (c) Component of heat flux in X-direction (copper sample)   (d) Component of heat flux in X-direction (alumina sample)
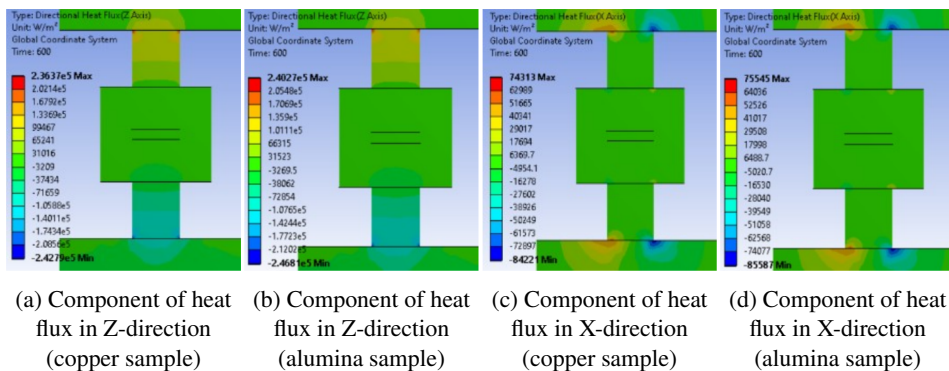
Fig. 11. Distributions of directional ("vertical" and "horizontal") heat fluxes in the die-punch-sample assembly calculated respectively for the copper and alumina samples at 600 s

the direction of circulation (flow) of the electric current in the machine. In the same sense, it should also be noted that the areas with a high variation in section cause an obstruction of thermal conduction; which will also push the heat flux to reach the highest values in these areas. Finally, it should be noted that the present study shows that the electrical resistivity is the most important parameter which makes it possible to obtain the highest temperature compared to the thermal conductivity.

4.2.2. Distributions of electric current density and electric field

Figs. 12 and 13 respectively show the "total" and "directional" electric current density distributions in the SPS device, calculated respectively for the cases of copper and alumina samples at 600 s. It can be seen that the total current density has a higher value in the copper sample compared to the alumina sample (Fig. 12a and 12b); this is due to the differences in electrical resistivities and electrical conductivities of copper and alumina. As well illustrated in the figures, the difference

| Cross-sectional view | 3D view | Cross-sectional view | 3D view |

(a) Copper sample   (b) Alumina sample

Fig. 12. Distributions of "total" electric current density in the die-punch-sample assembly calculated respectively for the (a) copper and (b) alumina samples at 600 s

(a) "Horizontal" current density (copper sample)   (b) "Horizontal" current density (alumina sample)   (c) "Vertical" current density (copper sample)   (d) "Vertical" current density (alumina sample)
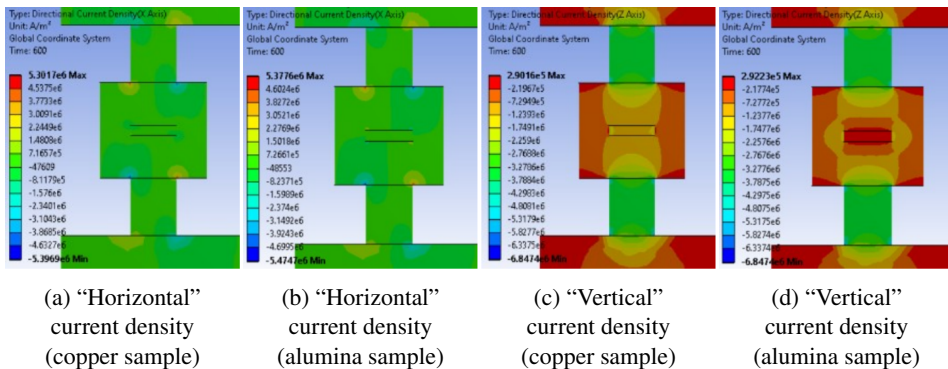
Fig. 13. Distributions of directional ("Horizontal" and "Vertical") electric current density in the die-punch-sample assembly calculated respectively for the copper and alumina samples at 600 s

in electric current density distribution only appears in the punch-die-sample assembly where the change in sample material has taken place. In addition, for both cases, due to the boundary conditions and the direction of movement of the electric current, it is found that the absolute value of the intensity of the vector of the current density (see Fig. 1) is greater in the vertical direction (Z-direction in Fig. 1) than in the horizontal direction (X-direction in Fig. 1) (see Fig. 13a, 13b, 13c and 13d). For example, in the vertical direction we see that the electric current passes freely through the copper sample (good electrical conductor) unlike the alumina which acts as an obstacle to the electric current (insulator).

Likewise, Fig. 14 shows the total electric field intensity distributions in the SPS device, calculated respectively for the copper and alumina samples at 600 s. It can be seen that there is a big difference between the two sampling cases, whether at the level of the values or at the level of the distribution model of the intensity of the electric field. This is quite obvious and expected since copper is a good electrical conductor compared to alumina (an insulator). Thus, for the case of the copper sample, the electric current circulates freely in the sample and the obstruction of the flow of the electric current will take place just at the level of the punch due to the large variation in section; this is why it is observed that the electric field intensity reaches the maximum values at the levels of the two punches. Whereas, in the case of the alumina sample, we have two obstacles to the circulation of the electric current which are the great variation of the section at the level of the punch and at the level of the sample itself; and in these two zones (punch and sample) we observe the maximum electric field intensity values.

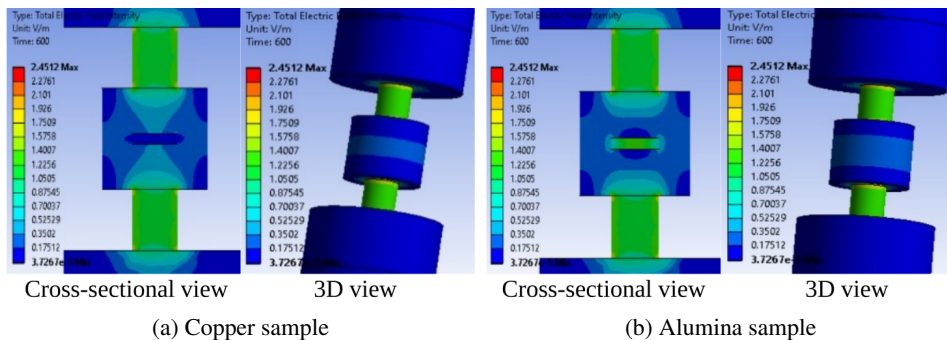| Cross-sectional view 3D view	Cross-sectional view 3D view
(a) Copper sample	(b) Alumina sample

Fig. 14. Distributions of total electric field intensity in the die-punch-sample assembly calculated respectively for the copper and alumina samples at 600 s

4.3. Effects of current and pressure applied to the SPS device on its thermoelectric and mechanical behavior

In this part, particular attention must be paid to determining the best *operating* conditions of the SPS device, which will make it possible to obtain a denser and more homogeneous product in a shorter time. This task consists in determining

the *optimal* current and pressure conditions applied to the SPS device. The determination of such conditions makes it possible to explain and justify the operating conditions used experimentally (1000 A and 8.72 MPa) in previous works. In order to carry out the above-mentioned task, it is necessary to study the effects of electric current and pressure applied to the system (SPS device) on its thermoelectric and mechanical behavior. We will perform numerical simulations in the following cases:

- **Case 1:** by fixing the applied pressure at 8.72 MPa and increasing the applied current to 1500 A then decreasing it to 500 A, and
- **Case 2:** by setting the applied current to 1000 A and decreasing the applied pressure to 5 MPa then increasing it to 15 MPa (see Table 5).

4.3.1. Thermoelectric behavior
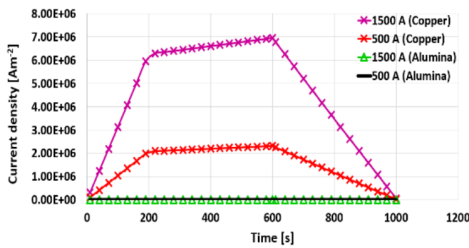
The curves in Fig. 15 show the time evolutions of the electric current density in the copper and alumina samples predicted for the two cases of applied current of 1500 and 500 A, respectively. Recall predictions were made for an applied pressure of 8.72 MPa (Case 1). For the case of the alumina sample, the current density is zero inside the sample for the two cases of applied current because alumina is an electrical insulator; whereas, in the case of the copper sample, the current density increases in the sample with increasing current because copper is a good electrical conductor.

The aforementioned changes in electrical current density will significantly affect heat fluxes and temperature distributions. Indeed, the curves of Fig. 16 show the time evolutions of the heat flux in the copper and alumina samples for the two cases of applied current of 1500 and 500 A (Case 1), respectively. It can be seen that the passage of electric current through the sample particularly affects the heat flux (due to the generation of heat by the Joule effect); in fact, when the applied current is multiplied by 3, the thermal flux increases approximately ten times in the case of the copper sample and approximately five times in the case of the alumina sample. Furthermore, the curves in Fig. 17 show the time evolutions of the temperature in the samples of copper and alumina predicted for the two cases of applied current of 1500 and 500 A (Case 1), respectively. It can be seen that contrary to the previous evolutions of the heat flux, which show higher values in the copper sample than in the alumina sample, the temperature evolution, however, reaches higher values in the alumina than in copper. Moreover, when the applied current is multiplied by 3, the temperature increases more than four times and it is higher in the case of alumina than in copper. We can therefore conclude here that not only the circulation of the electric current in the sample have an influence on the thermal behavior of the sample but also the electrical resistivity that it possesses is responsible for this behavior.

Table 5. Numerical experiments carried out to determine the optimal current and applied pressure conditions

Applied current [A]	Applied pressure, p [MPa]	Sample	Maximum Von Mises stress, $\sigma_{e\,max}$ [MPa]	Minimum Von Mises stress, $\sigma_{e\,min}$ [MPa]	Relative difference*	Maximum temperature, T_{max} [K]	Sample failure	Operating condition
Effect of applied electric current (Case 1)								
500	8.72	Alumina	193.05	18.278	90.531%	493.15	no	Acceptable
		Copper	**138.4**	**68.429**	**50.557%**	**490.29**	**no**	**Optimal**
1000	8.72	Alumina	454.52	83.026	81.733%	1061.9	no	Used in experiment [6]
		Copper	136.3	66.094	51.508%	1051.3	no	Used in experiment [6]
1500	8.72	Alumina	974.01	224.71	76.929%	1804.3	no	Acceptable
		Copper	133.87	63.031	52.916%	1787.6	yes (liquid phase)	Failure
Effect of applied pressure (Case 2)								
1000	5	**Alumina**	**488.36**	**109.88**	**77.500%**	**1061.9**	**no**	**Optimal**
		Copper	77.071	36.557	52.567%	1051.3	no	Acceptable
1000	8.72	Alumina	454.52	83.026	81.733%	1061.9	no	Used in experiment [6]
		Copper	136.3	66.094	51.508%	1051.3	no	Used in experiment [6]
1000	15	Alumina	461.13	38.615	91.626%	1061.9	no	Acceptable
		Copper	236.45***	115.96	50.957%	1051.3	yes (plastic)	Failure

* Relative difference = $\left| \left(\dfrac{\sigma_{e\,max} - \sigma_{e\,min}}{\sigma_{e\,max}} \right) \right|$,   ** Violation of the assumption "solid phase sintering"

*** Violation of the assumption: "elastic behavior of the sample"

T_m (alumina) = 2345 K, T_m (copper) = 1358 K,

Yield stress of copper $\sigma_{y,\,Cu}$ = 200 MPa,   Yield stress of alumina $\sigma_{y,\,Al2O3}$ = 1720 MPa

Fig. 15. Time evolutions of electric current density in copper and alumina samples predicted for the two applied cases of current 1500 and 500 A, respectively (Case 1)
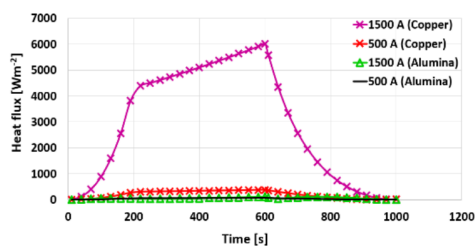

Fig. 16. Time evolutions of heat flux in copper and alumina samples predicted for the two cases of applied current 1500 and 500 A, respectively (Case 1)
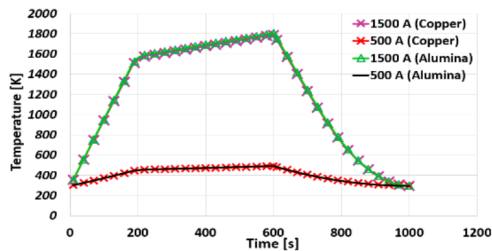

Fig. 17. Time evolutions of temperature in copper and alumina samples predicted for the two cases of applied current 1500 and 500 A, respectively (Case 1)

4.3.2. Mechanical behavior

Fig. 18 and 19 respectively show cross-sectional views of the "von Mises stress" and "equivalent" elastic strain distributions calculated in the copper and alumina samples at $t = 600$ s, respectively. The calculations were performed for (Case 1) and (Case 2) respectively, as shown in Table 5.

Discussion on determining the optimum applied current and pressure conditions
– Examination of the Fig. 18 and 19 shows that in all the cases studied "(Case 1) and (Case 2)", the maximum values of the stresses are located at the edges of the sample (regardless of the type of sample).

– Exposure of the studied samples to the conditions of cases 1 and 2 leads to very different patterns in the stress distributions in the sample. These models can be summarized as follows:

Copper under (Case 1 and Case 2) conditions
For the case of the copper sample, a large variation is observed in the stress values between the edges and the center of the sample when the electric current is high (Case 1 with 1500 A, see Fig. 18 and Table 5) or when applying low pressure (Case 2 with 5 MPa, see Fig. 19 and Table 5). However, in our case, the application of a high pressure of 15 MPa (Case 2) gave a high stress value (about 236 MPa), which is higher than the elastic limit of copper (see Table 5); this will guide us to

(a) Copper sample
(1500 A and 8.72 MPa)

(b) Copper sample
(1000 A and 8.72 MPa)

(c) Copper sample
(500 A and 8.72 MPa)

(d) Alumina sample
(1500 A and 8.72 MPa)

(e) Alumina sample
(1000 A and 8.72 MPa)
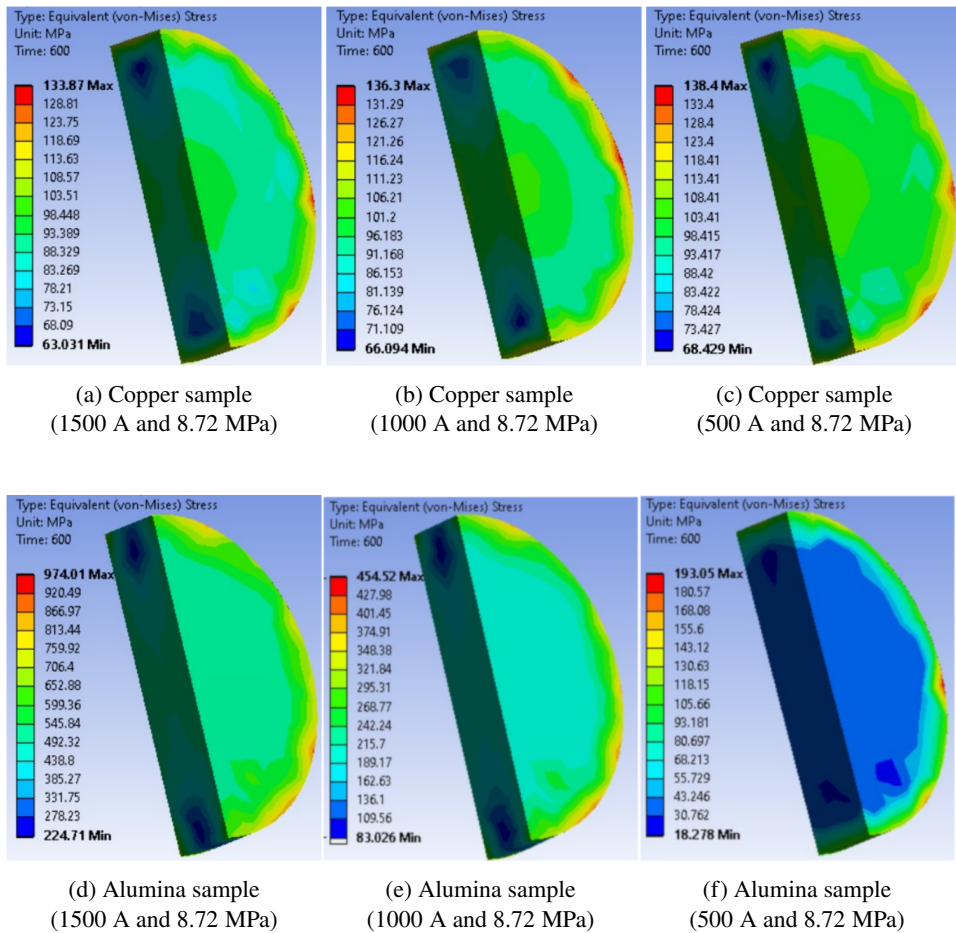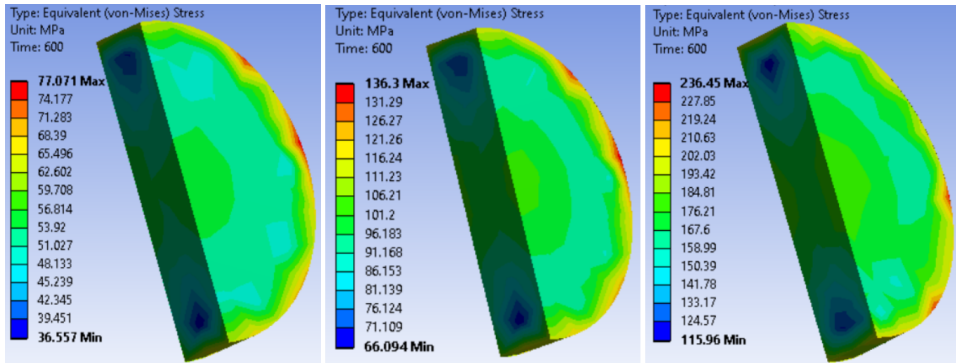
(f) Alumina sample
(500 A and 8.72 MPa)

Fig. 18. Cross-sectional views of von Mises stress distributions in copper and alumina samples at 600 s. The system is subjected to different intensities of electric current and the pressure is fixed at 8.72 MPa (Case 1)

keep the applied pressure value of 8.72 MPa and apply a current of 500 A as the best choices to have a better state (distribution) of stresses in the sample.

Alumina under (Case 1 and Case 2) conditions

For the case of the alumina sample, there is a large variation in the stress values between the edges and the center of the sample for the cases when the current of 500 A is applied (Case 1 with 500 A, see Fig. 18 and Table 5) and when the largest pressure value is applied (i.e., Case 2 with 15 MPa). Therefore, increasing the electric current and decreasing the applied pressure results in a better state of stress in the sample. However, in our case, the application of an electric current of 1500 A (Case 1) gave a high stress value (about 1185 MPa), which is considered unacceptable; this will guide us to keep the applied current value of 1000 A and the

(a) Copper sample
(1000 A and 5 MPa)

(b) Copper sample
(1000 A and 8.72 MPa)

(c) Copper sample
(1000 A and 15 MPa)
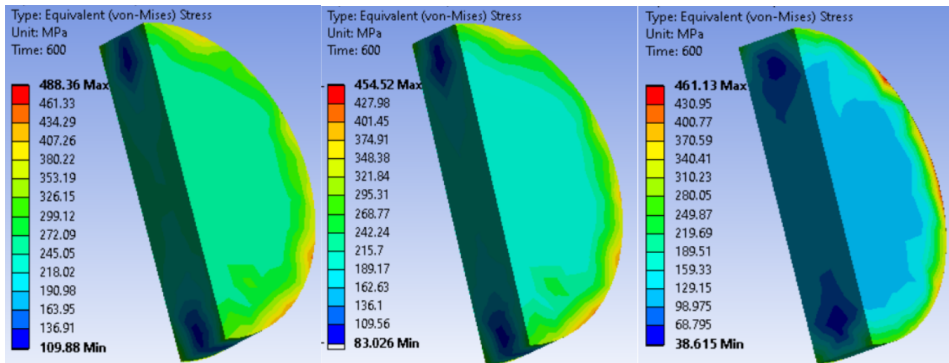
(d) Alumina sample
(1000 A and 5 MPa)

(e) Alumina sample
(1000 A and 8.72 MPa)

(f) Alumina sample
(1000 A and 15 MPa)

Fig. 19. Cross-sectional views of von Mises stress distributions in copper and alumina samples at
600 s. The system is subjected to different pressures and the current is fixed at 1000 A (Case 2)

applied pressure of 5 MPa as the best choices to have a better state (distribution)
of stress and strain in the alumina sample.

In conclusion,

In this part of the present work, the goal is to find the most homogeneous
distribution of stresses in the sample; we therefore conclude that the best conditions
for having a better state of stress are:

- An applied current of 1000 A and a pressure of 5 MPa are the best conditions
  for the alumina sample,

and

- An applied current of 500 A and a pressure of 8.72 MPa represent the best
  conditions for the copper sample.

5. Conclusions

Numerical simulations were performed to study the behavior of thermal, electrical and mechanical couplings. These physics are fully coupled during SPS sintering of ceramic and metallic materials. The first part of the study was carried out with the aim of highlighting the behavior of the coupling itself, while the second part investigates the effects of the key parameters (pressure and current applied) on the sintered material (product) in order to determine the optimal parameters leading to a better microstructure of the product. The determination of the optimal parameters is mainly based on the examination of the state of stress and strain in the sample.

The main conclusions of this study can be summarized as follows:

From the first part of the study:

- The flow of heat and the flow of electric current depend on the nature of the sample. Indeed, the electric current is denser in the copper sample than in the alumina sample; but this is not enough to have a higher temperature in copper than in alumina. This can be interpreted by the fact that although the thermal conductivity of the sample has a great influence on the distribution of the temperature field and the heat flux in the sample; but, its electrical resistivity is the most important parameter which plays the major role to get the maximum value of temperature in the sample. Therefore, electrical resistivity gives greater thermal stress in the alumina sample than in the copper sample.

- The stress distribution in the sample is controlled by the value of the Poisson's ratio. Indeed, the Poisson's ratio affects not only the increase in stresses in the radial direction but also the decrease in stresses in the axial direction.

- The coefficient of thermal expansion of the sample has an important effect and controls the distribution of mechanical strains in the sample.

From the second part of the study

- At a constant value of the applied current, the increase in the applied pressure does not affect the temperature field in the sample but it leads to an increase in the value of the stress in the sample but also its distribution is not homogeneous. However, with a constant value of the applied pressure, the increase in the applied electric current increases the temperature which in turn contributes to increasing the value of the stress in the sample but its distribution is not homogeneous.

- To have a more homogeneous material by the SPS method, it is necessary to take into account whether the sample is an electrically conductive or non-conductive material. Indeed, the flow of electric current in the sample has an important role in the characteristics obtained from the sample.

- The numerical study is in good agreement with the experiment. In fact, it shows that the best SPS conditions to have a more homogeneous material are

an input current of 1000 A and an applied pressure of 5 MPa for the alumina sample, an input current of 500 A and an applied pressure of 15 MPa for the copper sample.

References

[1] C. Wang, L. Cheng, and Z. Zhao. FEM analysis of the temperature and stress distribution in spark plasma sintering: Modelling and experimental validation. *Computational Materials Science*, 49(2):351–362, 2010. doi: 10.1016/j.commatsci.2010.05.021.

[2] M. Fattahi, M.N. Ershadi, M. Vajdi, F.S. Moghanlou, and A.S. Namini. On the simulation of spark plasma sintered TiB2 ultra high temperature ceramics: A numerical approach. *Ceramics International*, 46(10A):14787–14795, 2020. doi: 10.1016/j.ceramint.2020.03.003.

[3] A. Pavia, L. Durand, F. Ajustron, V. Bley, G. Chevallier, A. Peigney, and C. Estournès. Electro-thermal measurements and finite element method simulations of a spark plasma sintering device. *Journal of Materials Processing Technology*, 213(8):1327–1336, 2013. doi: 10.1016/j.jmatprotec.2013.02.003.

[4] E.A. Olevsky, C. Garcia-Cardona, W.L. Bradbury, C.D. Haines, D.G. Martin, and D. Kapoor. Fundamental aspects of spark plasma sintering: II. Finite element analysis of scalability. *Journal of the American Ceramics Society*, 95(8):2414–2422, 2012. doi: 10.1111/j.1551-2916.2012.05096.x.

[5] D. Tiwari, B. Basu, and K. Biswas. Simulation of thermal and electric field evolution during spark plasma sintering. *Ceramics International*, 35:699–708, 2009. doi: 10.1016/j.ceramint.2008.02.013

[6] X. Wang, S.R. Casolco, G. Xu, and J.E. Garay. Finite element modeling of electric current-activated sintering: The effect of coupled electrical potential, temperature and stress. *Acta Materialia*, 55(10):3611–3622, 2007. doi: 10.1016/j.actamat.2007.02.022.

[7] G. Maizza, S. Grasso, Y. Sakka, T. Noda, and O. Ohashi. Relation between microstructure, properties and spark plasma sintering (SPS) parameters of pure ultrafine WC powder. *Science and Technology of Advanced Materials*, 8(7-8):644–654, 2007. doi: 10.1016/j.stam.2007.09.002.

[8] G. Garcia and E. Olevsky. Numerical simulation of spark plasma sintering. *Advances in Science and Technology*, 63:58–61, 2010.doi: 10.4028/www.scientific.net/AST.63.58.

[9] K. Vanmeensel, A. Laptev, J. Hennicke, J. Vleugels, and O. Vanderbiest. Modelling of the temperature distribution during field assisted sintering. *Acta Materialia*, 53:4379–4388, 2005. doi: 10.1016/j.actamat.2005.05.042.

[10] A. Cincotti, A.M. Locci, R. Orrù, and G. Cao. Modeling of SPS apparatus: Temperature, current and strain distribution with no powders. *AIChE Journal*, 53(3):703–719, 2007. doi: 10.1002/aic.11102.

[11] A. Zavaliangos, J. Zhang, M. Krammer, and J. Groza. Temperature evolution during field activated sintering. *Materials Science and Engineering: A*, 379(1-2):218–228, 2004. doi: 10.1016/j.msea.2004.01.052.

[12] S. Muñoz and U. Anselmi-Tamburini. Temperature and stress fields evolution during spark plasma sintering processes. *Journal of Materials Science*, 45:6528–6539, 2010. doi: 10.1007/s10853-010-4742-7.

[13] C. Wolff, S. Mercier, H. Couque, and A.Molinari. Modeling of conventional hot compaction and Spark Plasma Sintering based on modified micromechanical models of porous materials. *Mechanics of Materials*, 49:72–91, 2012. doi: 10.1016/j.mechmat.2011.12.002.

[14] C. Manière, G. Lee, J. McKittrick, and E. Olevsky. Energy efficient spark plasma sintering: breaking the threshold of large dimension tooling energy consumption. *Journal of the American Ceramics Society*, 102(2):706–716, 2019. doi: 10.1111/jace.16046.

[15] W. Chen, U. Anselmi-Tamburini, J.E. Garay, J.R. Groza, and Z.A. Munir. Fundamental investigations on the spark plasma sintering/synthesis process I. Effect of dc pulsing on reactivity. *Materials Science and Engineering: A*, 394(1-2):132–138, 2005. doi: 10.1016/j.msea.2004.11.020.

[16] I. Sulima, G. Boczkal, and P. Palka. Mechanical properties of composites with titanium diboride fabricated by spark plasma sintering. *Archives of Metallurgy and Materials*, 62(3):1665–1671, 2017. doi: 10.1515/amm-2017-0255.

[17] D. Bubesh Kumar, B. Selva babu, K.M. Aravind Jerrin, N. Joseph, and A. Jiss. Review of spark plasma sintering process. *IOP Conference Series: Materials Science and Engineering*, 993:012004, 2020. doi: 10.1088/1757-899X/993/1/012004.

[18] P.Yu. Nikitin, I.A. Zhukov, and A.B. Vorozhtsov. Decomposition mechanism of AlMgB14 during the spark plasma sintering. *Journal of Materials Research and Technology*, 11:687–692, 2021. doi: 10.1016/j.jmrt.2021.01.044.

[19] M. Stuer, P. Bowen, and Z. Zhao. Spark plasma sintering of ceramics: from modeling to practice. *Ceramics*, 3(4):476–493, 2020. doi: 10.3390/ceramics3040039.

[20] U. Anselmi-Tamburini, S. Gennari, J.E. Garay, and Z.A. Munir. Fundamental investigations on the spark plasma sintering/synthesis process: II. Modeling of current and temperature distributions. *Materials Science and Engineering: A*, 394(1-2):139–148,2005. doi: 10.1016/j.msea.2004.11.019

[21] G. Lee, E. Olevsky, C. Manière, A. Maximenko, O. Izhvanov, C. Back, and J. McKittrick. Effect of electric current on densification behavior of conductive ceramic powders consolidated by spark plasma sintering. *Acta Materialia*, 144:524–533, 2017. doi: 10.1016/j.actamat.2017.11.010.

[22] A. Annamalai, M. Srikanth, A. Muthuchamy, S. Acharya, A. Khisti, D. Agrawal, and C. Jen. Spark plasma sintering and characterization of Al-TiB2 composites. *Metals*, 10(09):1110, 2020. doi: 10.3390/met10091110.

[23] G. Molenat, L. Durand, J. Galy, and A. Couret. Temperature control in spark plasma sintering: An FEM approach. *Journal of Metallurgy*, 2010:145431, 2020. doi: 10.1155/2010/145431.

[24] J. Gurt Santanach, A. Weibel, C. Estournès, Q. Yang, C. Laurent, and A.Peigney. Spark plasma sintering of alumina: Study of parameters, formal sintering analysis and hypotheses on the mechanism(s) involved in densification and grain growth. *Acta Materialia*, 59:1400–1408, 2011. doi: 10.1016/j.actamat.2010.11.002.

[25] S. Deng, R. Li, T. Yuan, and P. Cao. Effect of electric current on crystal orientation and its contribution to densification during spark plasma sintering. *Materials Letters*, 229:126–129, 2018. doi: 10.1016/j.matlet.2018.07.001.

[26] Z.A. Munir, U. Anselmi-Tamburini, and M. Ohyanagi. The effect of electric field and pressure on the synthesis and consolidation of materials: A review of the spark plasma sintering method. *Journal of Materials Science*, 41:763–777, 2006. doi: 10.1007/s10853-006-6555-2.

[27] S. Grasso, P. Poetschke, V. Richter, G. Maizza, Y. Sakka, and M. Reece. Low-temperature spark plasma sintering of pure nano WC powder. *Journal of the American Ceramic Society*, 96(6):1702–1705, 2013. doi: 10.1111/jace.12365.

[28] M.M. Shahraki, M.D. Chermahini, M. Abdollahi, R. Irankhah, P. Mahmoudi, and E. Karimi. Spark plasma sintering of SnO$_2$ based varistors. *Ceramics International*, 46(12):20429–20436, 2020. doi: 10.1016/j.ceramint.2020.05.135.

[29] F. Mechighel, G. Antou, B. Pateyron, A. Maître, and M. El Ganaoui. Simulation numérique du couplage électrique, thermique et mécanique lors du frittage "flash" de matériaux céramiques et métalliques. Congrès Français de Thermique/Actes, 2008. https://www.sft.asso.fr/document.php?pagendx=10430.

[30] F. Mechighel, A. Maître, B. Pateyron, M. El Ganaoui, and M. Kadja. Evolution de la température lors du processus du frittage "flash". Congrès Français de Thermique/Actes, 2009. https://www.sft.asso.fr/document.php?pagendx=9830.

[31] S.O. Jeje, M.B. Shongwe, A.L. Rominiyi, and P.A. Olubambi. Spark plasma sintering of titanium matrix composite – a review. *The International Journal of Advanced Manufacturing Technology*, 117:2529–2544, 2021. doi: 10.1007/s00170-021-07840-7.

[32] E. Bódis and Z. Károly. Fabrication of graded alumina by spark plasma sintering. *The International Journal of Advanced Manufacturing Technology*, 117:2835–2843, 2021. doi: 10.1007/s00170-021-07855-0.

[33] ANSYS software (16.2) [ANSYS Workbench]. (2015). https://www.ansys.com.

[34] R.J. Chowdhury. *Numerical Study of the Process Parameters in Spark Plasma Sintering (SPS)*. Master of Science Thesis, Faculty of the Graduate College of the Oklahoma State University, 2013.

[35] CES EduPack software, Granta Design Limited, Cambridge, UK (2019). Ansys (CES) Granta EduPack. https://www.ansys.com/products/materials/granta-edupack.

[36] F. Mechighel, M. El Ganaoui, M. Kadja, B. Pateyron, and S. Dost. Numerical simulation of three dimensional low Prandtl liquid flow in a parallelepiped cavity under an external magnetic field. *Fluid Dynamics & Materials Processing*, 5(4):313–330, 2009. doi: 10.3970/fdmp.2009.005.313.

[37] C. Manière, A. Pavia, L. Durand, G. Chevalier, K. Afanga, and C. Estournès. Finite-element modeling of the electro-thermal contacts in the spark plasma sintering process. *Journal of the European Ceramic Society*, 36(3):741–748, 2016. doi: 10.1016/j.jeurceramsoc.2015.10.033.

[38] G. Antou, G. Mathieu, G. Trolliard, and A. Maître. Spark plasma sintering of zirconium carbide and oxycarbide: Finite element modeling of current density, temperature, and stress distributions. *Journal of Materials Research*, 24:404–414, 2009. doi: 10.1557/JMR.2009.0039.

[39] K.N. Zhu, A. Godfrey, N. Hansen, and X.D. Zhang. Microstructure and mechanical strength of near- and sub-micrometre grain size copper prepared by spark plasma sintering. *Materials & Design*, 117:95–103, 2017. doi: 10.1016/j.matdes.2016.12.042.

[40] C. Arnaud, C. Manière, G. Chevallier, C. Estournès, R. Mainguy, F. Lecouturier, D. Mesguich, A. Weibel, L. Durand, and C. Laurent. Dog-bone copper specimens prepared by one-step spark plasma sintering. *Journal of Materials Science*, 50:7364–7373, 2015. doi: 10.1007/s10853-015-9293-5.

[41] J. Diatta, G. Antou, N. Pradeilles, and A. Maître. Numerical modeling of spark plasma sintering – Discussion on densification mechanism identification and generated porosity gradients. *Journal of the European Ceramic Society* 37(15):4849–4860, 2017. doi: 10.1016/j.jeurceramsoc.2017.06.052.